Indian Journal of Engineering

Numerical simulation of the arm length effect of an octo-copter

Saoussane Gouiaa[☼]**, Ameni Mehdi, Zied Driss, Bilel Ben Amira, Mohamed Salah Abid**

Laboratory of Electro-Mechanic Systems (LASEM), National School of Engineers of Sfax (ENIS), University of Sfax, B.P. 1173, km 3.5 Soukra, 3038 Sfax, TUNISIA

[☼]**Corresponding author:**
Laboratory of Electro-Mechanic Systems (LASEM),
National School of Engineers of Sfax (ENIS),
Univrsity of Sfax,
B.P. 1173, km 3.5 Soukra, 3038 Sfax,
TUNISIA
E-mail address: saoussane1918gouia@gmail.com; saoussane.gouiaa@enis.tn (S. Gouiaa).

General Note
Article is recommended to print as color digital version in recycled paper.

ABSTRACT

The evolution of the UAVs leads to the creation of new configuration of multi-copters. This type of aircrafts has many advantages especially in civil and military applications because it can be used in high risk situations without endangering a human life and inaccessible areas. In this paper, a computer simulation has been investigated to study the aerodynamic structure around a

configuration of multi-copters named octo-copter X8. This type of UAVs has eight rotors. Every two rotors are coaxial. The numerical model used is based on the Navier-Stokes equations with a k-ε turbulence model. The resolution of these equations is based on the finite volume discretization. We have varied the length of the arm of the octo-copter and we have extracted the local characteristics of every aerodynamic structure using the software "Solidworks Flow Simulation" in order to determine the best octo-copter based on the stability criterion.

**Keywords:** computer simulations, octo-copter, aerodynamic structure, CFD.

1. INTRODUCTION

In the last decades, academic and industrial applications have generated a big interest on the use of UAVs because of their capability to work in hard conditions where the surrounding environment is dangerous like in the case of civil and especially military applications [1-2]. There are a wide range of UAVs. The first type is the plane using the lift power of the wing to maintain itself in the air [3]. Another used type of UAVs is the VTOL aircrafts and helicopter is an important configuration of it. A helicopter is an aerodynamic aircraft which is designed to take off and land vertically, hover in the air and move to any direction. Necessary lifting force and thrust are created by one or more rotors, driven by reciprocating or jet engines. The classical scheme of a helicopter: one large main rotor on top and a tail rotor to compensate the reactive moment [4-5]. The widespread type is the multi-rotors or the multi-copters. A particular case of helicopters is a flying platform with 3–6 or 4–8 and more rotors [6]. This type, in addition to its important advantages, presents many problems especially in the stability of flying and the low efficiency of its propellers. So, many researchers used numerical simulations to solve these problems. For example, Shi et al. [7] used numerical simulations to predict the aerodynamic flow around helicopter rotors in hover. Strawn et al. [8] presents highlights from CFD modeling and development of aircrafts. Caradonna et al. [9] presented the experimental and analytical studies of a model helicopter rotor in hover. Ansari et al. [10] cited new approaches from previous literature, classified them into many types like steady-state, quasi-steady and fully unsteady methods used in the aerodynamic modeling for micro-air vehicles. From the mentioned references, it appears clearly that the design of the aircraft, the geometrical parameters and the external conditions have a big effect on the aerodynamic behavior of the aircraft. In this paper, we are interested on the study of the aerodynamic structure around an octo-copter.

2. GEOMETRICAL ARRANGEMENT

Figure 1 presents the chosen geometrical model. It is an octo-copter drone with coaxial propellers. Each two propellers are mounted on a motor to facilitate the design. We choose to work with X5C-02 main blades propeller because it is the type of rotors available in our laboratory. Figure 1.a shows the geometrical arrangements of the model, defined by a diameter of the propeller d=135 mm, a length of the arm L=135 mm, L=210 mm and L=285 mm, a length of the support ls and a radius of the support R.

Figure 1.b presents its exploded view. The white propeller is a Clockwise CW propeller and the red propeller is a Counter Clockwise CCW propeller. Considering that the coaxial octo-copter can fly if each two opposite propellers rotate at the same direction, each two adjacent propellers should rotate at different direction and the upper of the octo-copter should have the opposite configuration of the bottom. The propellers are also fixed considering their availability in the laboratory. So, we have studied the effect of the variation of the arm's length. In fact, we have changed the prototype arm-length to obtain the most accurate configuration which met the goals. The sizes of the arm's length are equal to L=135 mm, L=210 mm and L=285 mm. Figure 2 shows the 3D presentation in each case of study.
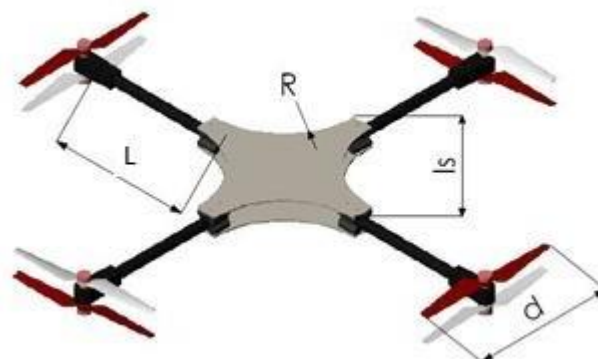
(a) Geometrical arrangements of the model
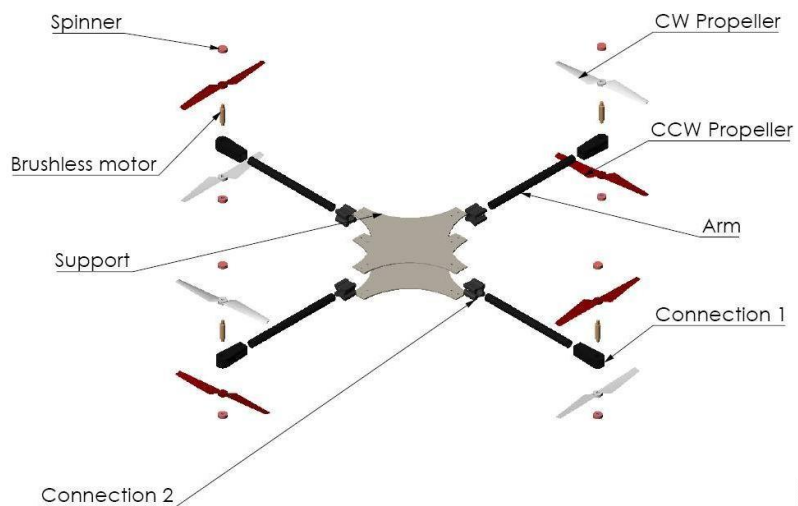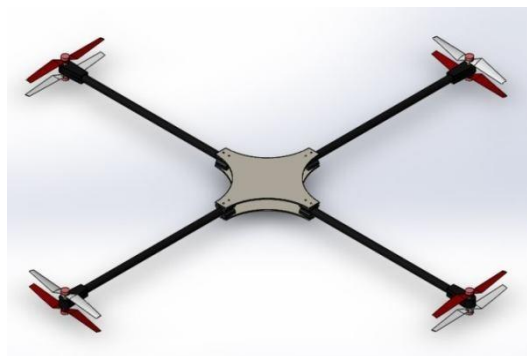
(b) Exploded view of the geometrical model

Figure 1 Geometrical model

(a) L = 135 mm

(b) L = 210 mm

(c)

L = 285 mm

Figure 2 3D case study

3. NUMERICAL MODEL

To study the aerodynamic structure around an octo-copter, a computer simulation has been done. The used software is "Solidworks Flow Simulation". This software is based on the resolution of the Navier-Stokes equations with a k-ε turbulence model [11-12]. The resolution of these equations is based on the finite volume discretization [13-14]. The spatial discretization is obtained by following a procedure for tetrahedral interpolation scheme. For the temporal discretization, the implicit formulation is adopted.

3.1. Control volume and boundary conditions

Figure 3 shows a presentation of the control volume depicted with the boundary conditions. The pressure is equal to p=101325 Pa and the air molecular mass is equal to 0.029 kg/mol. Each one of the three octo-copters rotates in a rotational speed equal to Ω=1711 rpm. The boundary conditions are the presented in the form of the wall limiting the control volume. This model gives us the most accurate values of force and local characteristics.
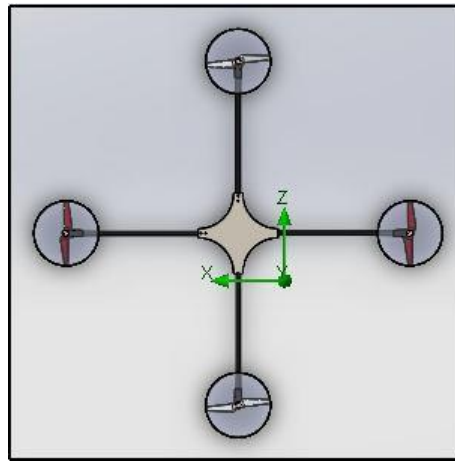

Figure 3 Control volume

3.2. Mesh resolution

In this section, we have created a rotating flow simulation study by selecting a new project using wizard, adjusting the domain size, setting initial and local initial mesh, creating a rotating region and setting up the goals. In order to carry out the numerical simulations, it is important to set the mesh in every case of study. Figure 4 shows the chosen mesh types for the three cases. We fixed an unstructured mesh having the characteristics shown in table 1.
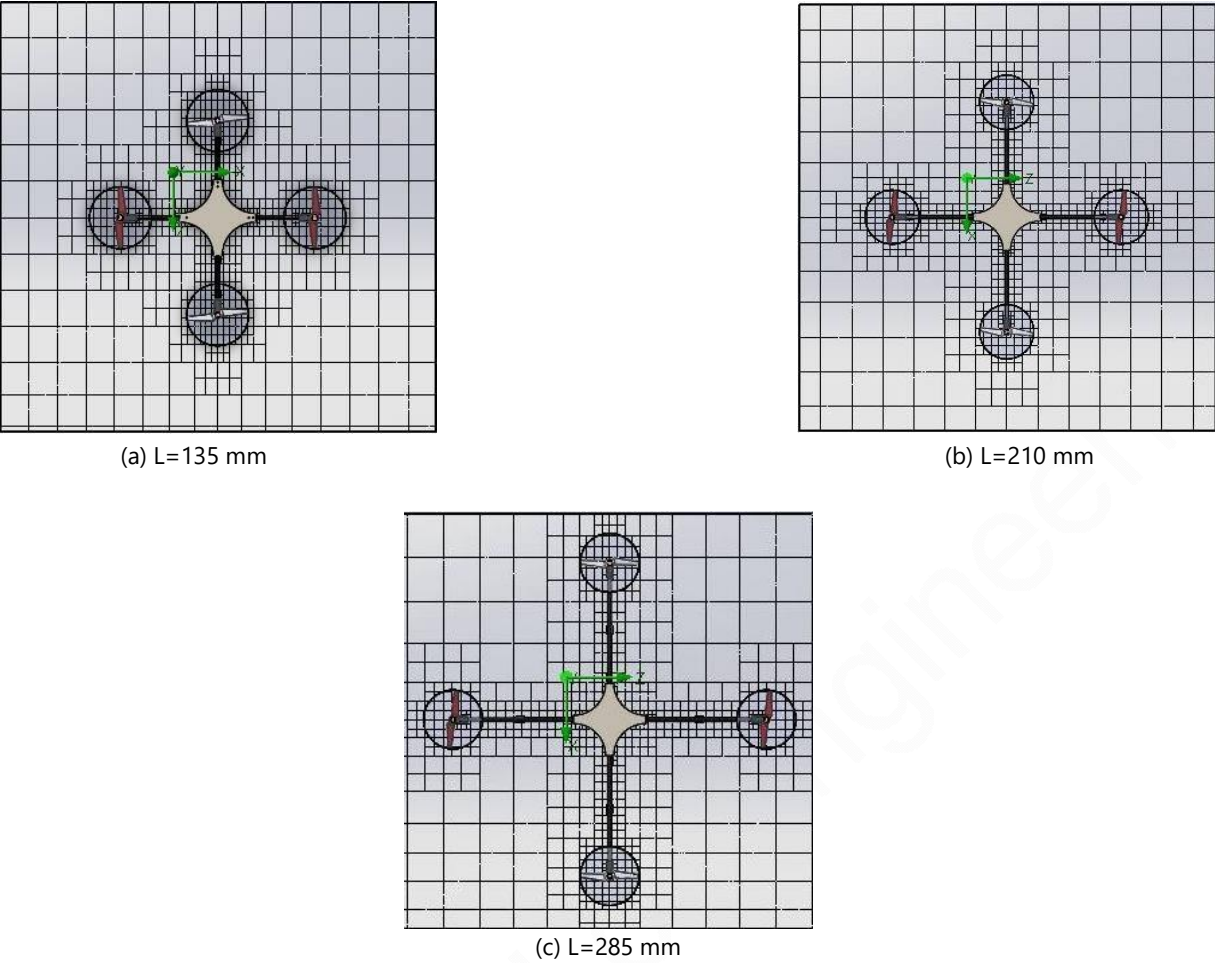
(a) L=135 mm

(b) L=210 mm

(c) L=285 mm

Figure 4 Different meshes used in the numerical models

Table 1 Selected mesh

Length	Number of fluid cells	Number of partial cells
L = 135 mm	10646	4368
L = 210 mm	9351	3738
L = 285 mm	10002	4573

3.3. Mathematical formulation

The model is based on the Navier-Stokes equations [11] presented by the following formulation:

$$\frac{\partial \rho}{\partial t} + \frac{\partial (\rho u_i)}{\partial x_i} = 0 \tag{1}$$

$$\frac{\partial (\rho u_i)}{\partial t} + \frac{\partial (\rho u_i u_j)}{\partial x_i} + \frac{\partial p}{\partial x_i} = \frac{\partial}{\partial x_j} (\tau_{ij} + \tau_{ij}^R) + S_i \tag{2}$$

Where:

ρ is the density (kgm^{-3}), t is the time (s), x_i and x_j are the Cartesian coordinates, u_i and u_j are the velocity components (ms^{-1}) respectively on the i and j directions, p is the pressure (Pa), S_i is the mass-distributed external force per unit mass (kg m^{-2}s^{-2}), T_{ij} is the viscous shear stress tensor (Pa).

In the case of Newtonian fluids, the viscous shear stress sensor is defined as:

$$T_{ij} = \mu\left(\frac{\partial u_i}{\partial x_j} + \frac{\partial u_j}{\partial x_i} - \frac{2}{3}\delta_{ij}\frac{\partial u_k}{\partial x_k}\right) \qquad (3)$$

μ is the viscosity (Pa s) and δ_{ij} is the Kronecker delta function.

Following Boussinesq assumption, the Reynolds-stress tensor has the form:

$$T_{ij}^R = \mu_t\left(\frac{\partial u_i}{\partial x_j} + \frac{\partial u_j}{\partial x_i} - \frac{2}{3}\delta_{ij}\frac{\partial u_k}{\partial x_k}\right) - \frac{2}{3}\rho k\delta_{ij} \qquad (4)$$

$$\mu_t = f_u\frac{C_u\rho k^2}{\varepsilon} \qquad (5)$$

$$f_u = [1 - \exp(-0.025Ry)]^2\left(1 + \frac{20.5}{R_T}\right) \qquad (6)$$

$$R_T = \frac{\rho k^2}{\mu\varepsilon} \qquad (7)$$

$$Ry = \frac{\rho\sqrt{k}y}{\mu} \qquad (8)$$

Where μ_t is defined using two basic turbulence properties: the turbulence kinetic energy k (J.kg^{-1}) and the turbulent dissipation ε (W kg^{-1}), f_u is the turbulent viscosity factor and y is the distance from the wall.

The two additional transport equations used to describe the turbulent kinetic energy and dissipation are presented as follows:

$$\frac{\partial(\rho k)}{\partial t} + \frac{\partial(\rho u_i k)}{\partial x_i} = \frac{\partial}{\partial x_i}\left[(\mu + \frac{\mu_t}{\sigma_k})\frac{\partial k}{\partial x_j}\right] + S_k \qquad (9)$$

$$\frac{\partial(\rho\varepsilon)}{\partial t} + \frac{\partial(\rho u_i\varepsilon)}{\partial x_i} = \frac{\partial}{\partial x_i}\left[(\mu + \frac{\mu_t}{\sigma_\varepsilon})\frac{\partial\varepsilon}{\partial x_j}\right] + S_\varepsilon \qquad (10)$$

Where S_k and S_ε are defined as:

$$S_k = T_{ij}^R\frac{\partial u_i}{\partial x_j} - \rho\varepsilon + \mu_t + P_B \qquad (11)$$

$$S_{\varepsilon} = C_{\varepsilon 1} \frac{\varepsilon}{k} (f_1 T_{ij} R \frac{\partial u_i}{\partial u_j} + \mu C_B P_B) - C_{\varepsilon 2} f_2 \frac{\rho \varepsilon^2}{k} \tag{12}$$

Here P_B represents the turbulent generation due to buoyancy forces and can be written as:

$$P_B = - \frac{g_i}{\sigma_B} \frac{1}{\rho} \frac{\partial \rho}{\partial x_i} \tag{13}$$

Where g_i is the component of gravitational acceleration in direction x_i, the constants σ_B, C_μ, $C_{\varepsilon 1}$, $C_{\varepsilon 2}$, σ_ε and σ_k are determined empirically and have these values: σ_B= 0.9, C_μ=0.09, $C_{\varepsilon 1}$ =1.44, $C_{\varepsilon 2}$ =1.92, σ_ε =1.3, σ_k =1.

C_B is defined by C_B=1 when P_B>0 and 0 otherwise;

$$f_1 = 1 + (\frac{0.05}{f\mu})^3 \tag{14}$$

$$f_2 = 1 - \exp(-R_T{}^2) \tag{15}$$

4. NUMERICAL RESULTS

In this section, four planes defined by x=0 mm, y=0 mm, y=112 mm and z=0 mm are considered to extract the necessary local characteristics. Particularly, we are interested on the distribution of the average velocity, the static pressure, the turbulent kinetic energy, the dissipation rate of the turbulent kinetic energy and the turbulent viscosity.
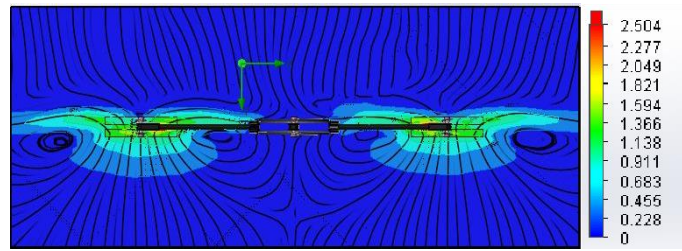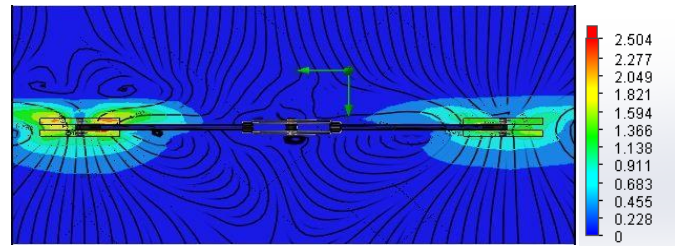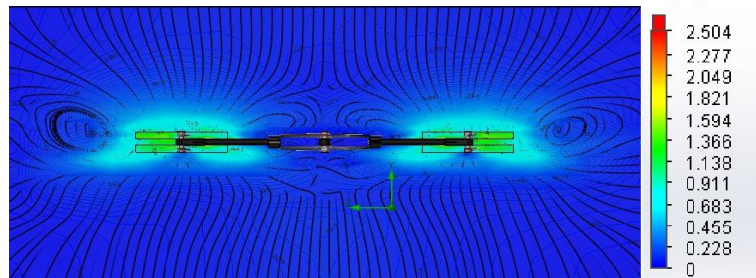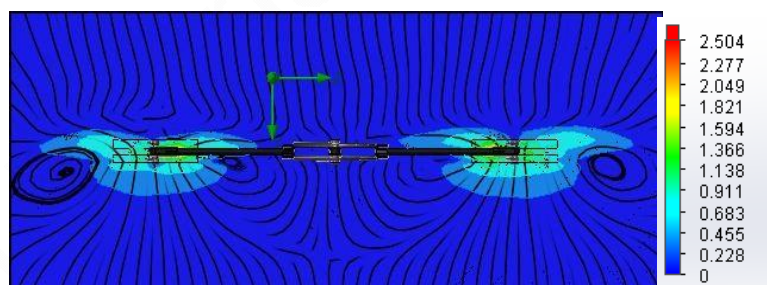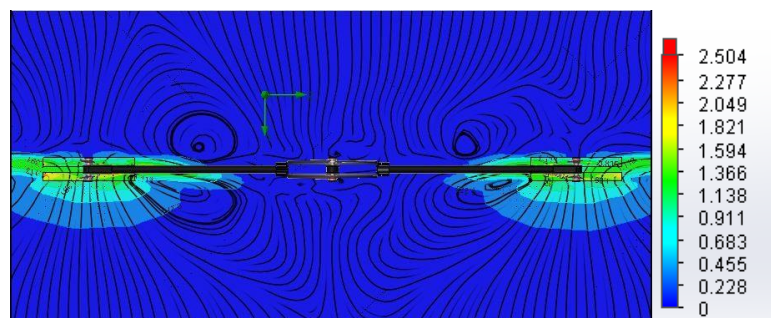
4.1. Average velocity

Figures 5, 6, 7 and 8 present the distribution of the average velocity in the visualization planes defined by x=0 mm, y= 0mm, y=112 mm and z=0 mm. In each plane, it has been observed the effect of the variation of the arm's length on the average velocity. According to these results, it has been noted that the average velocity is important near the propeller and decreases far from it in the three cases. Also, it has been observed that the high average velocity is concentrated in the upper surface of each propeller. When comparing the three cases, it is clear that, the more the length of the arm increases, the more the average velocity has a low value in the neighborhoods of the rotating volume of each rotor. The trajectories of stream lines shown in each plane present a big difference between the three cases. The vortex is far from the support of the drone in the case of L = 135 mm. The second and the third cases present more turbulent trajectories which mean less stability.
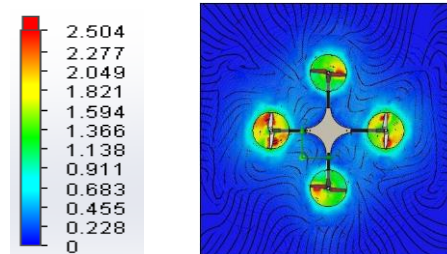
(a) L=135 mm
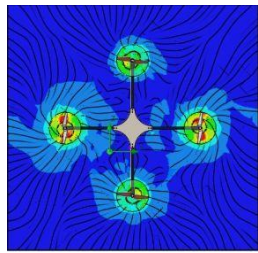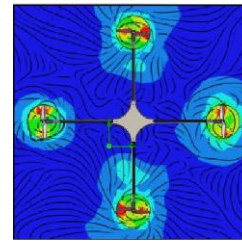
(b) L=210 mm

(c) L=285 mm

Figure 5 Distribution of the magnitude velocity in the plane y=0 mm
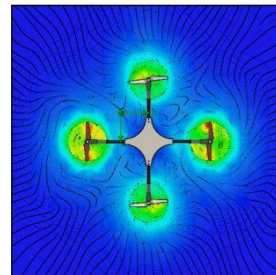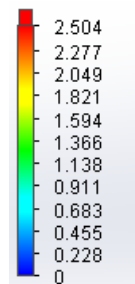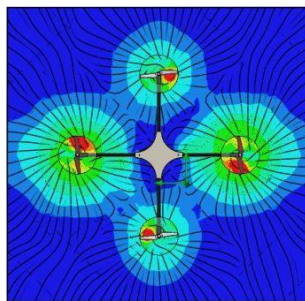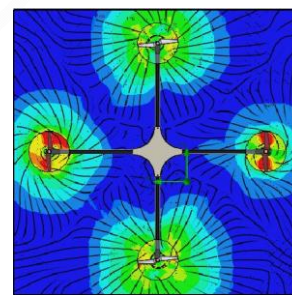
(a) L=135 mm

(b) L=210 mm

(c) L=285 mm

Figure 6 Distribution of the magnitude velocity in the plane y=112 mm
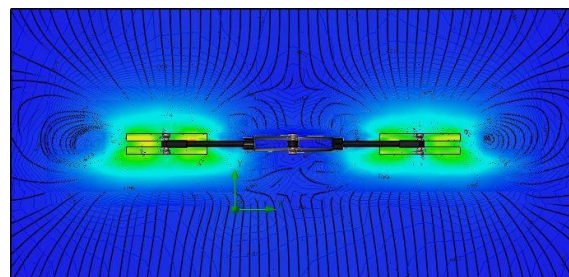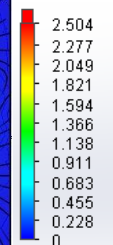
(a) L=135 mm

(b) L=210 mm

(c) L=285 mm

Figure 7 Distribution of the magnitude velocity in the plane z=0 mm

(a) L=135 mm

(b) L=210 mm

(c) L=285 mm

Figure 8 Distribution of the magnitude velocity in the plane x=0 mm

4.2. Static pressure

Figures 9, 10, 11 and 12 present the distribution of the static pressure in the visualization planes defined by x=0 mm, y=0 mm, y=112 mm and z=0 mm. In each plane, it has been observed the effect of the variation of the arm's length on the distribution of the static pressure. According to these results, it has been noted that the high pressure is concentrated in the rotating volume and decreases far from it in each rotor. Indeed, it has been observed that in the planes z=0 mm and x=0 mm, the higher pressure is located in the bottom of the octo-copter. However, its top is characterized by a low value of pressure. When comparing the three cases, it has been noted that the increment of the length of the arm increases also the zones of high pressure especially near the support of the drone. It has been noted that the distribution of the static pressure presented in each plane have a difference between the three cases. The compression zone near the support of the second and third octo-copter is higher than the one in the first octo-copter which means more stability.
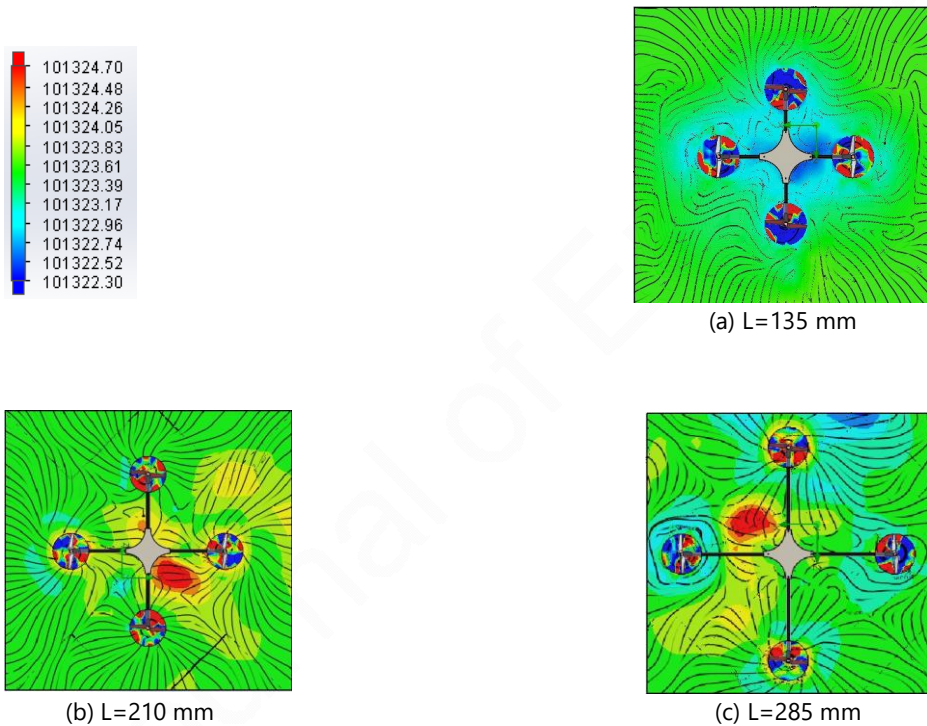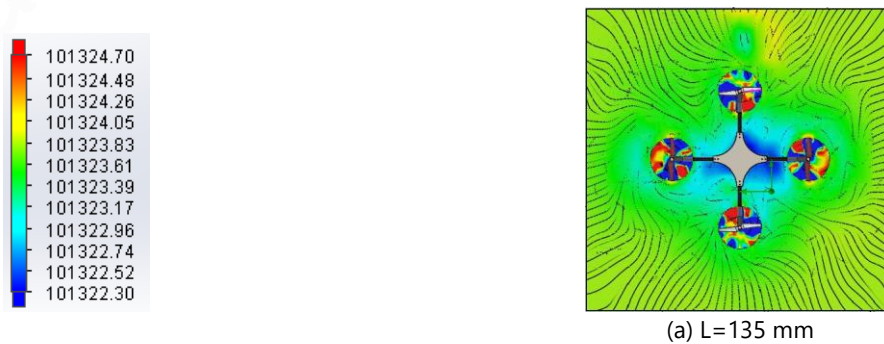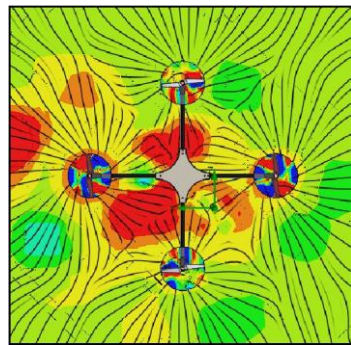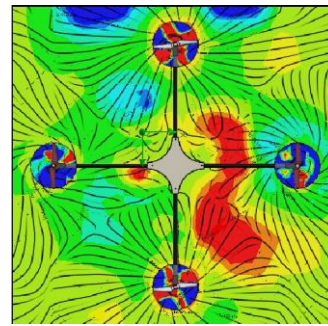

(a) L=135 mm

(b) L=210 mm

(c) L=285 mm

Figure 9 Distribution of the static pressure in the plane y=0 mm
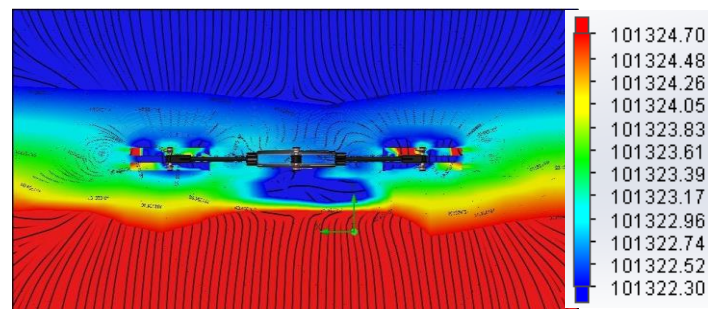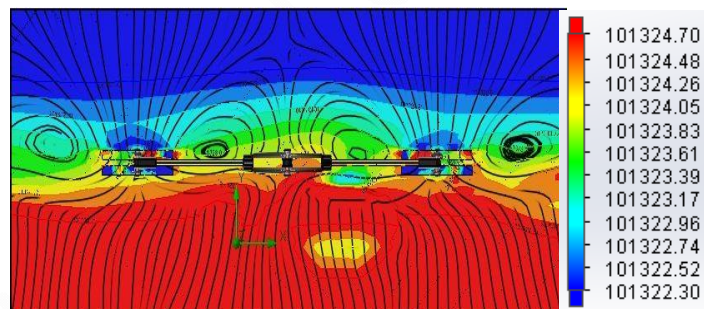

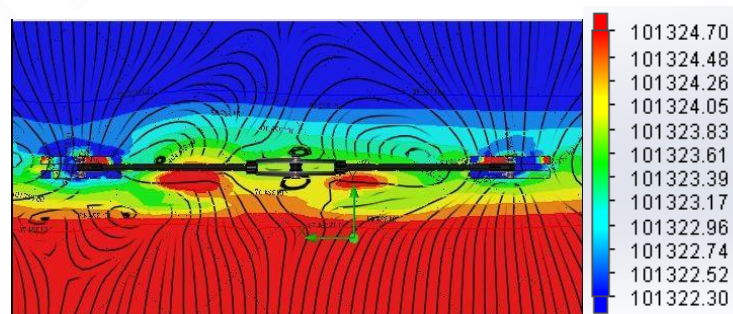(a) L=135 mm

(b) L=210 mm

(c) L=285 mm

Figure 10 Distribution of the static pressure in the plane y=112 mm

(a) L=135 mm

(b) L=210 mm

(c) L=285 mm

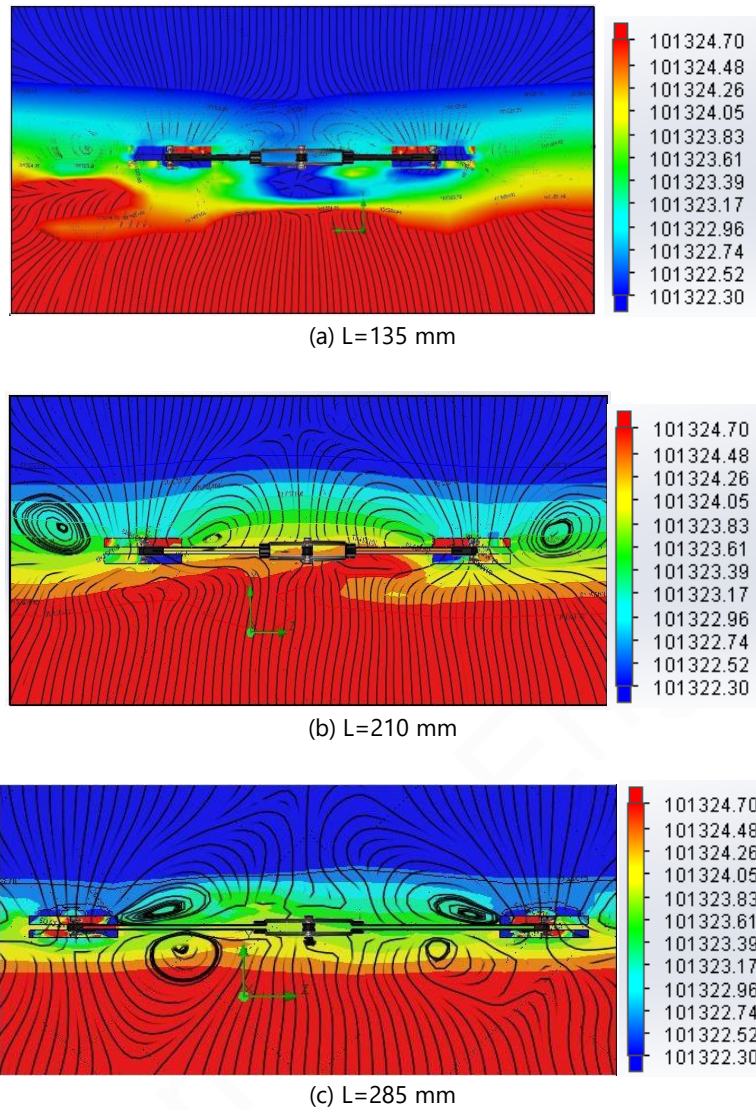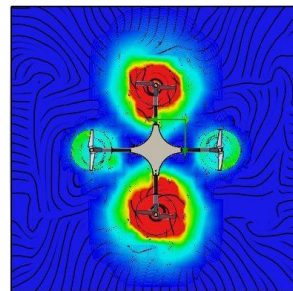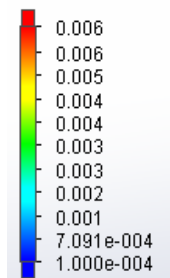**Figure 11** Distribution of the static pressure in the plane z=0 mm
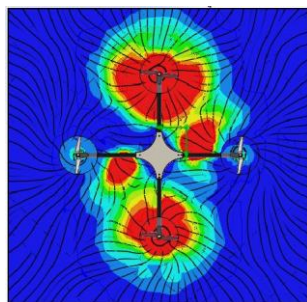
(a) L=135 mm

(b) L=210 mm

(c) L=285 mm

Figure 12 Distribution of the static pressure in the plane x=0 mm
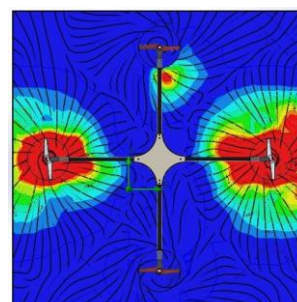
4.3. Turbulent kinetic energy

Figures 13, 14, 15 and 16 present the distribution of the turbulent kinetic energy in the visualization planes defined by x=0 mm, y=0 mm, y=112 mm and z=0 mm. In each plane, it has been observed the effect of the variation of the arm's length on the distribution of the turbulent kinetic energy. According to these results, it has been noted that in the plane y=112 mm, the turbulent kinetic energy is concentrated in the two red propellers contrarily to the two others that have a little variation of this parameter. This fact is inversed in the second plane. From the comparison of the three cases, it has been noted that the variation of the turbulent kinetic energy depends with the variation of the length of the arm. Indeed, it has been observed a high value of this parameter in the second and the third cases of study. Also, the trajectories of turbulence shown in each plane present a big difference between the three cases. The trajectories of the turbulence present more vortex far from the support of the drone in the case of L=135 mm which presents more stability.
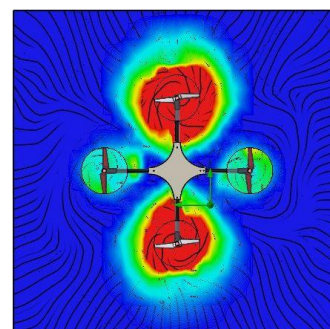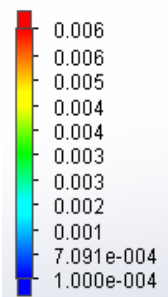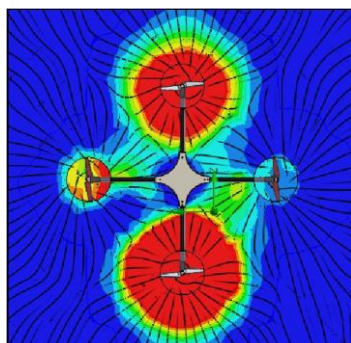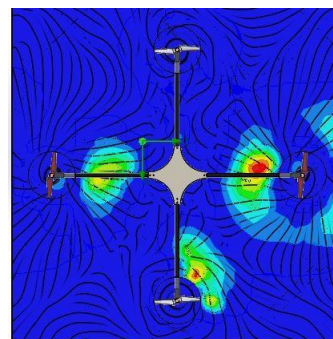
(a) L=135 mm

(b) L=210 mm

(c) L=285 mm

Figure 13 Distribution of the turbulent kinetic energy in the plane y=0 mm

(a) L=135 mm

(b) L=210 mm

(c) L=285 mm

Figure 14 Distribution of the turbulent kinetic energy in the plane y=112 mm

(a) L=135 mm

(b) L=210 mm

(c) L=285 mm

Figure 15 Distribution of the turbulent kinetic energy in the plane z=0 mm
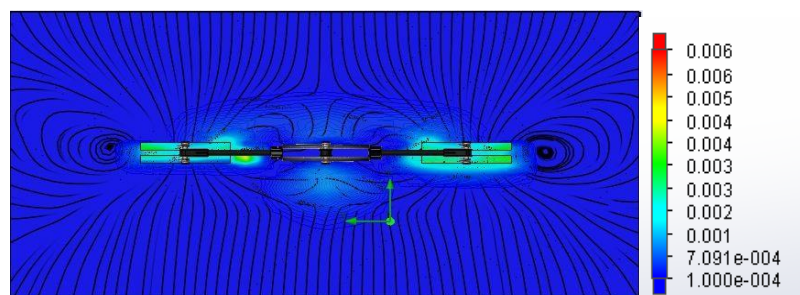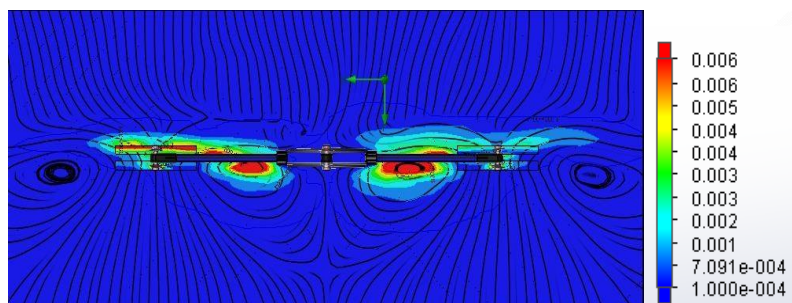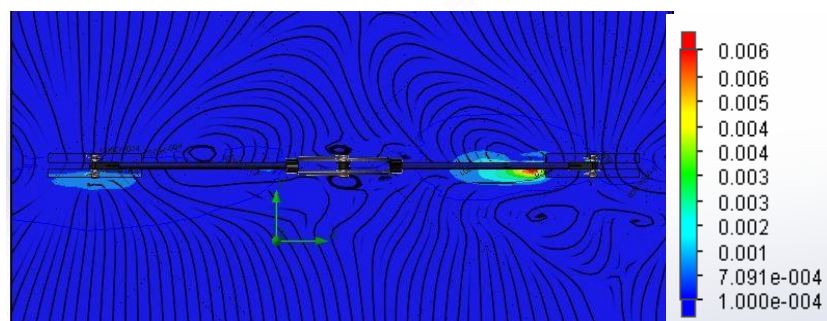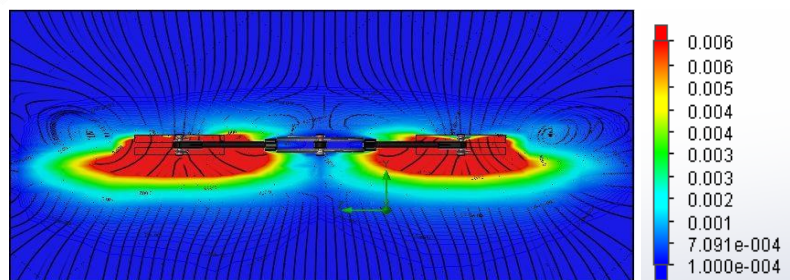

(a) L=135 mm
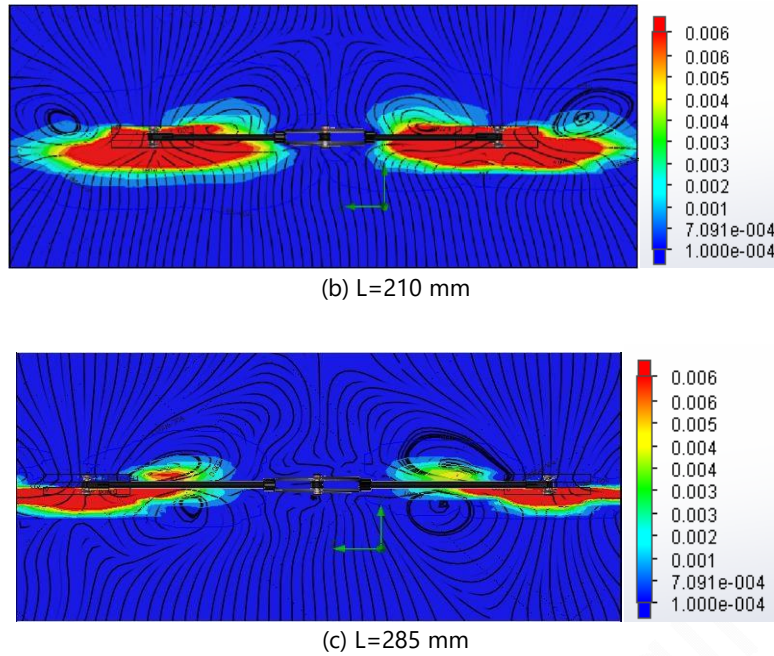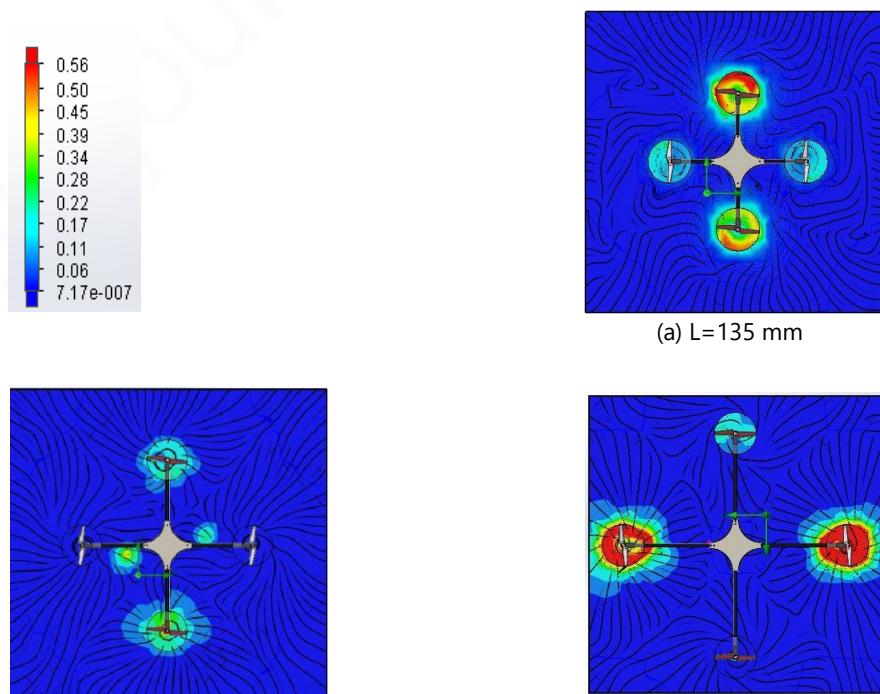
(b) L=210 mm

(c) L=285 mm

Figure 16 Distribution of the turbulent kinetic energy in the plane x=0 mm
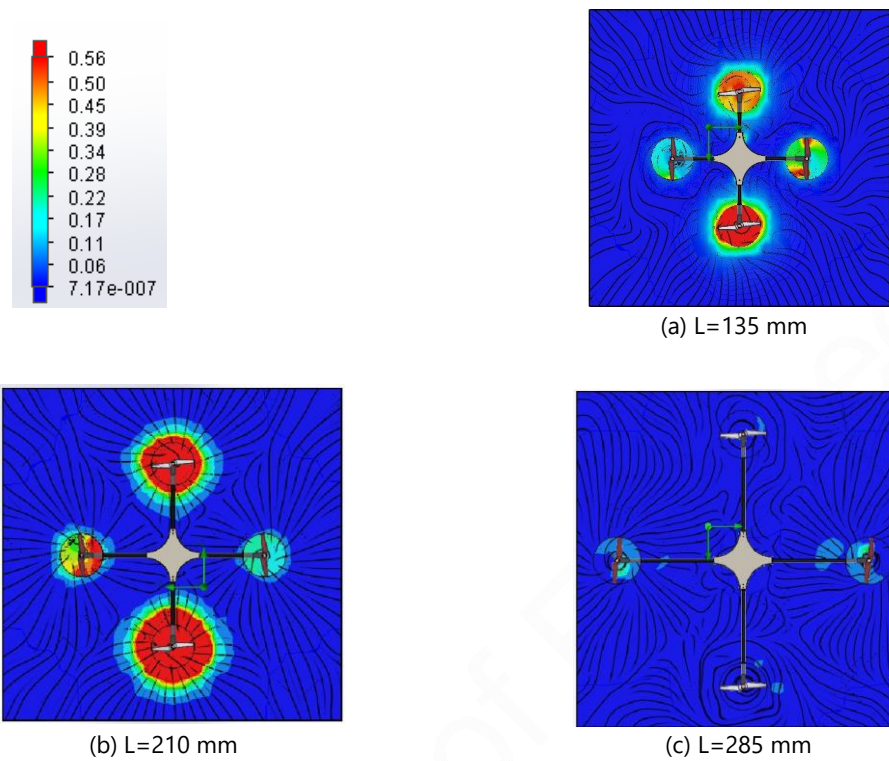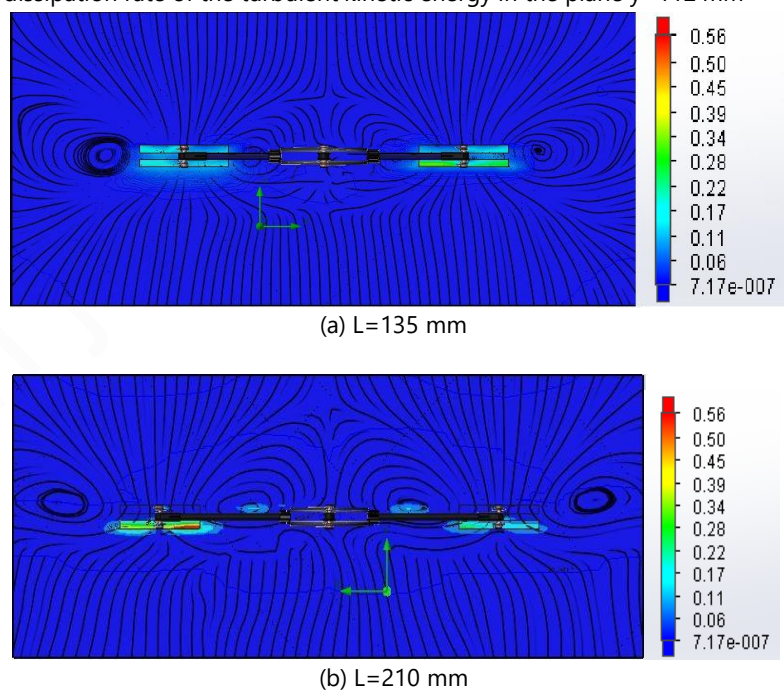
4.4. Dissipation rate of the turbulent kinetic energy

Figures 17, 18, 19 and 20 present the distribution of the dissipation rate of the turbulent kinetic energy in the visualization planes defined by x=0 mm, y=0 mm, y=112 mm and z=0 mm. In each plane, it has been observed the effect of the variation of the arm's length on the distribution of the dissipation rate of the turbulent kinetic energy. According to these results, it has been noted that the variation of the dissipation rate of the turbulent kinetic energy is located essentially at the level of the propellers. The plane z = 0 mm shows that it is concentrated in the inferior half of the octo-copter. Indeed, it has been observed that the regions where the turbulent kinetic energy is high have also a high values of the dissipation rate of the turbulent kinetic energy. When comparing the three cases, it has been noted that the turbulent dissipation rate depends on the length of the arm. The more the length increases, the more the dissipation rate of the turbulent kinetic energy increases too. When comparing the different trajectories of turbulence shown in the three cases, it is clear that the first case defined by L=135 mm is more stable.

(a) L=135 mm

(b) L=210 mm   (c) L=285 mm

Figure 17 Distribution of the dissipation rate of the turbulent kinetic energy in the plane y=0 mm

(a) L=135 mm

(b) L=210 mm   (c) L=285 mm

Figure 18 Distribution of the dissipation rate of the turbulent kinetic energy in the plane y=112 mm

(a) L=135 mm

(b) L=210 mm

(c) L=285 mm

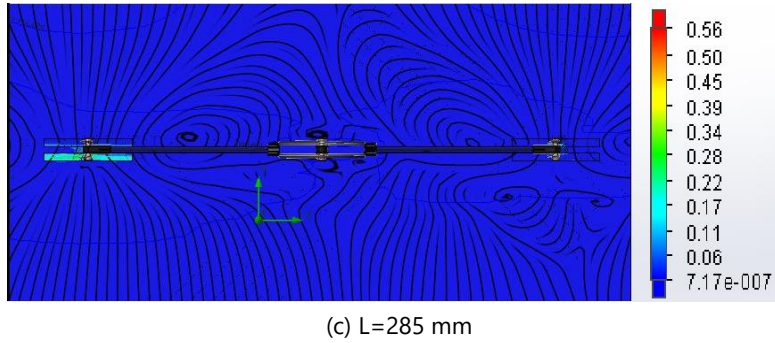**Figure 19** Distribution of the dissipation rate of the turbulent kinetic energy in the plane z=0 mm
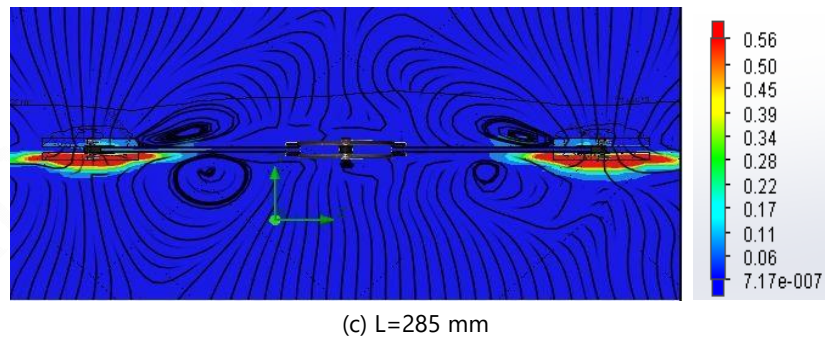

(a) L=135 mm

(b) L=210 mm

(c) L=285 mm
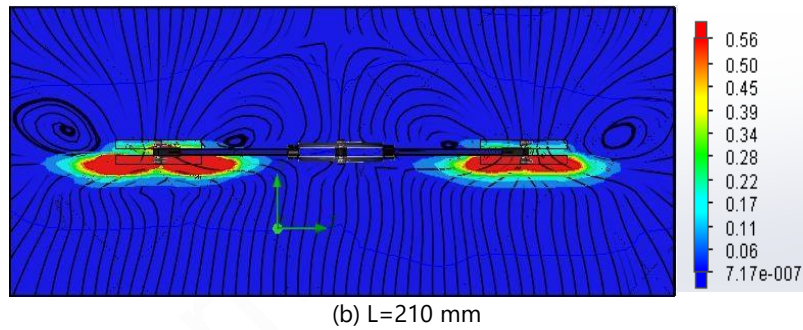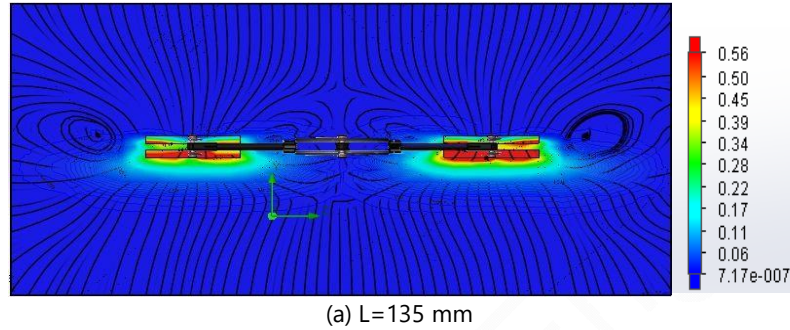
Figure 20 Distribution of the dissipation rate of the turbulent kinetic energy in the plane x=0 mm

4.5 Turbulent viscosity

Figures 21, 22, 23 and 24 present the distribution of the turbulent viscosity in the visualization planes defined by x=0 mm, y=0 mm, y=112 mm and z=0 mm. In each plane, it has been observed the effect of the variation of the arm's length on the distribution of the turbulent viscosity. According to these results, it has been noted that the high value of the turbulent viscosity is concentrated in the rotating volume of the propeller and in his neighborhood. The plane x = 0 mm shows that the high value of the turbulent viscosity is situated in the bottom of the octo-copter. The more the turbulent viscosity is approached to its top, the more it decreases. When

making a comparison between the three cases, it has been observed that the second and the third cases do not include any variation of the turbulent viscosity. Which means that the increment of the length of the arm decreases the value of the turbulent viscosity, even eliminates it. Also, the trajectories of stream lines shown in each plane present a big difference between the three cases.

(a) L=135 mm
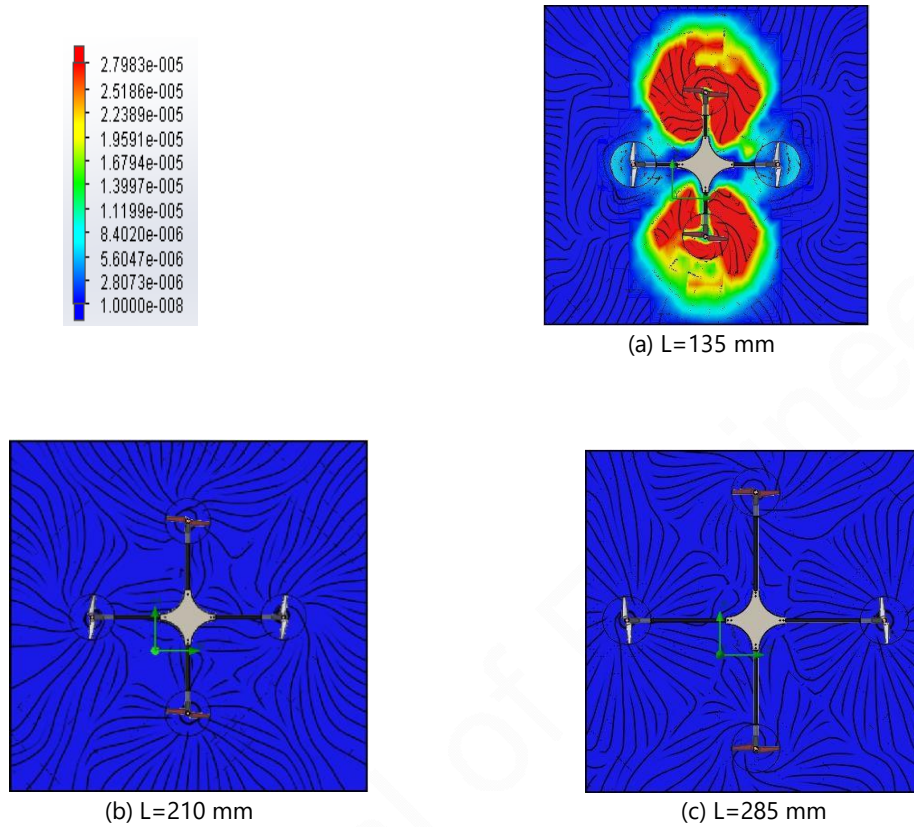
(b) L=210 mm

(c) L=285 mm

Figure 21 Distribution of the turbulent viscosity in the plane y=0 mm
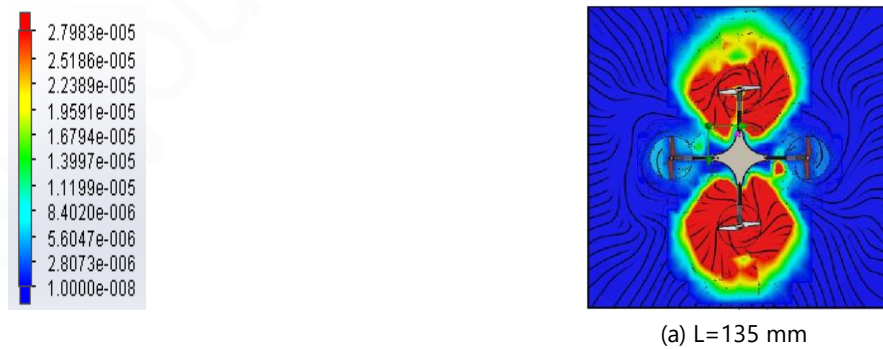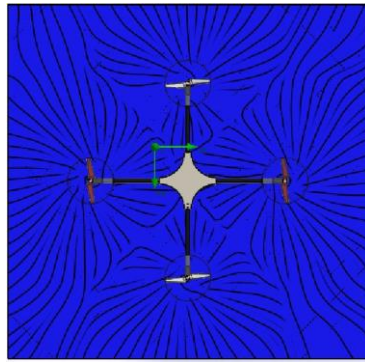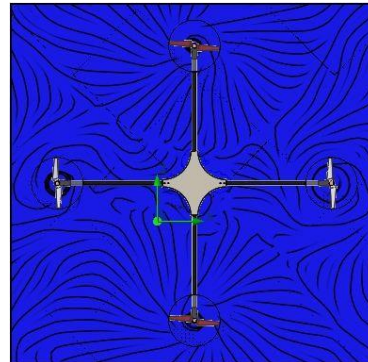
(a) L=135 mm

(b) L = 210 mm   (c) L = 285 mm

Figure 22 Distribution of the turbulent viscosity in the plane y=112 mm
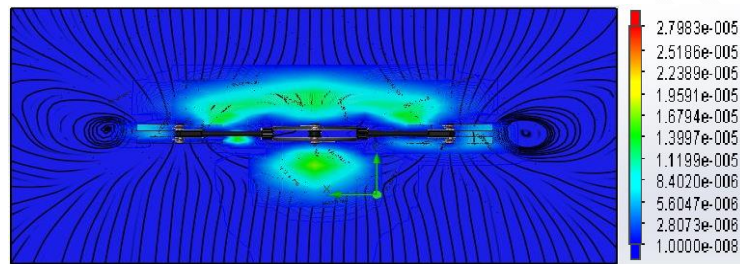
(a) L=135 mm
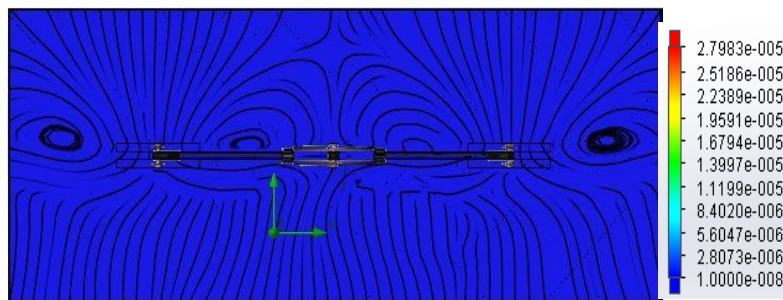
(b) L=210 mm
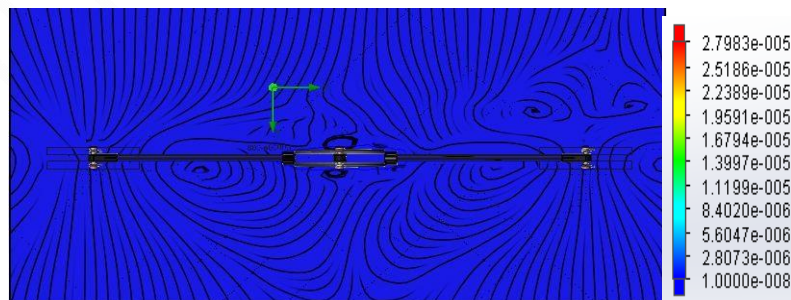
(c) L=285 mm

Figure 23 Distribution of the turbulent viscosity in the plane z=0 mm

(a) L=135 mm

(b) L=210 mm

(c) L=285 mm
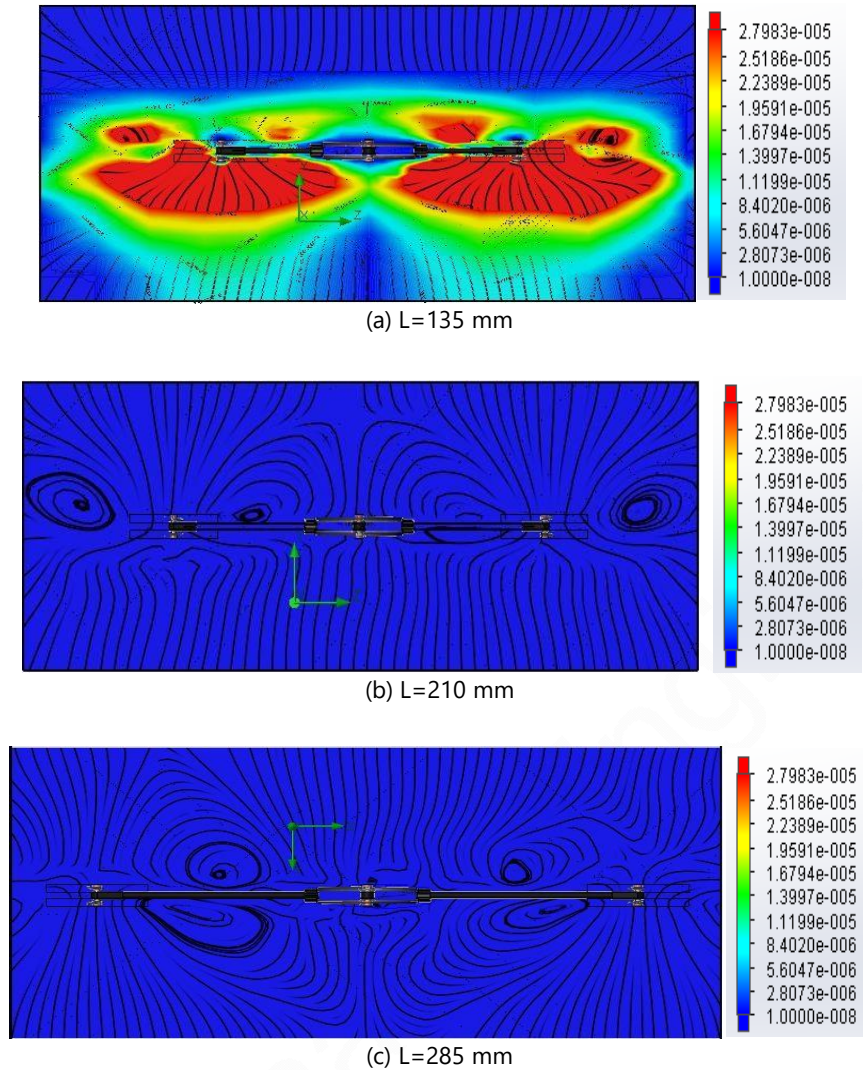
Figure 24 Distribution of the turbulent viscosity in the plane x=0 mm

4.6 Thrust force

Table 2 presents a comparison between the value of thrust force in the three cases of study and the experimental one. It has been noted that the more the value of the arm-length increases, the more the value of the average thrust force decreases. In our case, there is not a big difference between the values of thrust force in each case. When seeing the results, it has been noted that the experimental value of the force is near to the value of the first case of the study corresponding to the length L=135 mm.

Table 2 Thrust force values

| Case 1	0.081 N
Case 2	0.067 N
Case 3	0.056 N
Experimental value	0.078 N

5. CHOICE OF THE PROTOTYPE

Figure 25 shows a 3D presentation of the final presentation of the octo-copter with the chosen length of the arm. This choice was made via making a compromise between the local results especially the turbulence characteristics and the value of the produced thrust. After this study, it has been noted that the octo-copter having an arm's length equal to L = 135 mm is the most suitable. In fact, according to the turbulent trajectories located in every plane, it has been noted that in the second case, the vortex is far from

the support of the octo-copter. As a consequence, the stability of the octo-copter will increase compared to the two other cases. It is true that the first case has the highest value of thrust, but it presents many zones of instability.
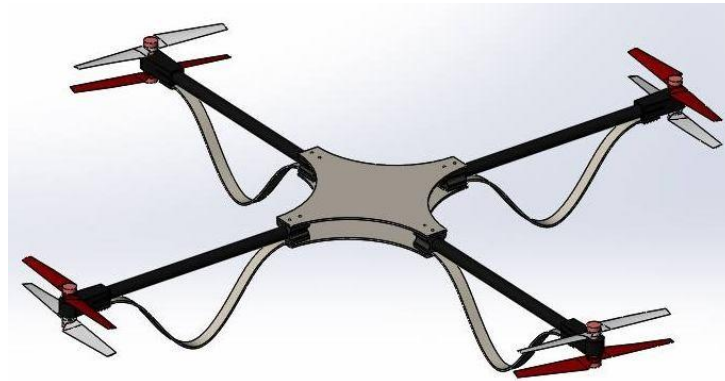

Figure 25 Presentation of the final prototype

9. CONCLUSION

The present paper shows simulation results applied for the prediction of the thrust. As the design of the frame is important to maximize the thrust and decrease the dissipation rate of the turbulent kinetic energy, the choice of the geometric model is required. At the beginning, we presented the proposed geometrical model of octo-copter with the three lengths of arms. Then, we have extracted the characteristics of the local results which are the average velocity, the static pressure, the turbulent kinetic energy, the dissipation rate of the turbulent kinetic energy and the turbulent viscosity in each case of study. According to the local results, we confirm that the adequate length can be determined by a compromising between the value of thrust and the stability, which means that the adequate frame size is the first one with L=135 mm. Indeed, it is the only case presenting vortex far from the support of the octo-copter which means that it is the only case that can fly with stability.

NOMENCLATURE

d: Diameter of the propeller (mm)
L: Length of the arm of the octo-copter (mm)
ls: Length of the support (mm)
R : Radius of the support (mm)
CW: Clockwise propeller
CCW: Counter Clockwise propeller
Ω: Rotational speed (rpm)
ρ : Density (kgm^{-3}),
t : Time (s)
x_i and x_j : Cartesian coordinates
u_i and u_j: Velocity components (ms^{-1}) respectively on the i and j directions
p : Pressure (Pa)
S_i : Mass-distributed external force per unit mass (kg m^{-2}s^{-2})
τ_{ij} : Viscous shear stress tensor (Pa)
μ : Viscosity (Pa s) δ_{ij} is the
δ_{ij} : Kronecker delta function
μ_t : Defined using k and ε
k: Turbulence kinetic energy (J.kg^{-1})
ε : Turbulent dissipation (W kg^{-1})
f_u : Turbulent viscosity factor

y: Distance from the wall

P_B : Turbulent generation due to buoyancy forces

g_i: Component of gravitational acceleration in direction x_i

$\sigma_B = 0.9$

$C_\mu = 0.09$

$C_{\varepsilon 1} = 1.44$

$C_{\varepsilon 2} = 1.92$

$\sigma_\varepsilon = 1.3$

$\sigma_k = 1$

REFERENCE

1. Erbil M. A., Prior S. D., Karamanoglu M., Odedra S., Barlow C., Lewis D., Reconfigurable unmanned aerial vehicles, Proceedings of the International Conference on Manufacturing and Engineering Systems, 2009, 392 – 421.

2. Current and future UAV military users and applications, Air & Space Europe, 1999, Vol. 1– 5, No. 6, 51 – 58.

3. Frulla G., Cestino E., Design, manufacturing and testing of a HALE-UAV structural demonstrator, Composite Structures, 2008, Vol. 83, 143 – 153.

4. Gavrilets V., Shterenberg A., Dahleh M.A., Feron E., Avionics system for a small unmanned helicopter performing aggressive maneuvers, Proceedings of 19th Digital Avionics Systems Conference, Philadelphia, USA, 2000, 1 – 7.

5. Taha Z., Tang Y.R., Yap K.C., Development of an onboard system for flight data collection of a small-scale UAV helicopter, Mechatronics, 2011, Vol. 21, 132 – 144.

6. Yoo D., Oh H., Won D., Tahk M., Dynamic modeling and stabilization techniques for tri-rotor unmanned aerial vehicles, International Journal of Aeronautical & Space Science, 2010, Vol. 11, No. 3, 167 – 174.

7. Shi Y., Zhao Q., Fan F., Xu G., A new single-blade hybrid CFD method for hovering and forward-flight rotor computation, Chinese Journal of Aeronautics 24(2011) 127-135.

8. Strawn R.C., Caradonna F.X., Duque E.P.N, 30 years of rotorcraft computational Fluid Dynamics research and development, Journal of the American Helicopter Society, 2005.

9. Caradonna F.X., Tung C., Experimental and analytical studies of a model helicopter rotor in hover, Vertica, Vol. 5, (2), 1981, pp. 149-161.

10. Ansari S., Zbikwoski R., Knowles K., Aerodynamic modeling of insect-like flapping flight for micro air vehicles, Progress in Aerospace Sciences 42(2006), 129-172.

11. Driss S., Driss Z., Kallel Kammoun I., Computational study and experimental validation of the heat ventilation in a living room with a solar patio system, Energy and Buildings, pp.28-40, Vol.119, 2016.

12. Driss Z., Mlayah O., Driss S., Driss D., Maaloul M., Abid M.S., Study of the bucket design effect on the turbulent flow around unconventional Savonious wind rotors, Energy, pp. 708-729, Vol. 89, 2015.

13. Bouabidi A., Driss Z., Cherif N., Abid M.S., Computational investigation of the external excitation frequency effect on liquid sloshing phenomenon, WSEAS Transactions on Fluid Mechanics, pp. 1-9, Volume 11, 2016.

14. Driss Z., Mlayah O., Driss S., Maaloul M., Abid M.S., Study of the incidence angle effect on the aerodynamic structure characteristics of an incurved Savonious wind rotor placed in a wind tunnel, Energy, pp.894-908, Vol 113, 2016.